

## MODELING AND MULTI-OBJECTIVE DESIGN OPTIMIZATION OF QUASI-CONTINUOUS HIGH MAGNETIC FIELD SYSTEMS

Huan Li<sup>1, 2</sup> and Hongfa Ding<sup>1, 2, \*</sup>

<sup>1</sup>Wuhan National High Magnetic Field Center, Huazhong University of Science and Technology, Wuhan, China

<sup>2</sup>State Key Laboratory of Advanced Electromagnetic Engineering and Technology, Huazhong University of Science and Technology, Wuhan, China

**Abstract**—This paper proposes a coupling model of the Quasi-Continuous High Magnetic Field (QCHMF) systems that incorporates the electrical, thermal and mechanical dynamics of the magnet system and the power supply system. The design of QCHMF systems is formulated as a five-objective optimization problem and a scoring system based on preference of the designer is adopted to classify the Pareto points of the optimization problem. An optimized mono-coil 50 T/100 ms QCHMF system is designed with a 67.5 MW rectifier of the Wuhan National High Magnetic Field Center (WHMFC), which is taken as an example to verify the proposed model and optimization method. Detailed simulation models of the optimized QCHMF system are built in Matlab and Comsol and the results agree well with the designed technical specifications. The proposed model and optimization method are generic which can be applied to other QCHMF systems with minor modifications.

### 1. INTRODUCTION

QCHMF magnet is a special kind of magnet that can sustain a high field, usually over 45 T, for a 0.1 s flat top or more. QCHMF can provide high accuracy quasi-continuous field at a relatively low cost for many experiments traditionally carried out in continuous magnetic fields [1–3]. However, due to the long pulse time and the high current, both the maximum power and consumed energy of the QCHMF

---

*Received 16 March 2013, Accepted 25 April 2013, Scheduled 30 April 2013*

\* Corresponding author: Hongfa Ding (dinghf@tom.com).

magnet are usually very high which are easy to exceed the power and energy limits of the power supply. Meanwhile, the high field level and the long pulse time will cause high temperature rise and magnetic force. Magnet failures happen if the temperature or the force exceeds the limits of the materials. Therefor the design of QCHMF magnet is a multi-objective optimization problem constrained by the temperature rise, the magnetic force, the level of processing and the capacity of the power supply. Moreover, some of these constraints are conflicting. For example, the temperature rise can be reduced with a larger volume of the magnet, but a larger volume usually results in high consumed power and energy which may exceed the limits of the power supply. All above make the design of QCHMF system be a complex coupling problem where tedious iterations are usually required. Up to now, many countries such as the Netherlands [4], the USA [5,6] and Austria [7] have carried out a lot of researches on QCHMF. A 60 T/0.1 s QCHMF has been achieved in the USA but the magnet is powered by a huge 1.43 GVA pulse generator which is beyond competition. The peak field of QCHMF systems at the Netherlands and Austria are both 40 T which are mainly constrained by the limited power supply capacity. Therefore, how to satisfy all the constraints and obtain the highest QCHMF within the limited capacities of the power supply is an important problem. To solve this problem, this paper presents a global coupling model of QCHMF systems that incorporates the mathematical model and operating characteristics of the QCHMF power supply system and the nonlinear model of the quasi-continuous magnet. Based on the models, the design of QCHMF systems is formulated as a five-objective optimization problem. A set of preferences are introduced to classify each point of the Pareto front. Based on the preferences, a scoring system is established to get a total score of each point. According to the score, a visualization technique is adopted to help find the optimized design of the multi-objective optimization problem.

With the proposed model and optimization method, an optimized 50 T/0.1 s QCHMF system is designed with the 67.5 MW 12-pulse rectifier of the WHMFC, which is taken as an example to verify the proposed model and optimization method. To verify the optimized design, Matlab/Simulink and Comsol 3.5a are adopted to build simulation models of the power supply system and the magnet. Simulation results showed that both the magnet and the power supply system have sufficient margin to achieve the designed 50 T/0.1 s QCHMF.

2. MATHEMATICAL MODEL OF THE POWER SUPPLY

2.1. Introduction of the Power Supply System

The power supply of QCHMF systems requires a very high power as well as high energy during a short pulse. Generally, there are two kinds of power supplies used in QCHMF systems: commercial utility grids and pulsed generator. However, the high pulsed power may cause some disturbances to utility grids. Therefore independent pulsed generators instead of utility grids are often utilized because they can store the energy in advance and discharge it during the pulse. Therefore independent pulsed generators instead of utility grid are often used as the power supply because they can store the energy in advance and discharge it during the pulse. To achieve the flat top, rectifiers are required to get a controlled DC voltage for the magnet. However, there is usually a relatively large reactance of the pulsed generator and the rotor speed decreases when the pulsed generator is powering the magnet. The large reactance and decrease of rotor speed will reduce the output capacity of the generator-rectifier power supply system. Therefore this paper uses the generator-rectifier power supply at the WHMFC as an example to illustrate the modeling method of the QCHMF power supply systems.

Figure 1 shows the circuit diagram of the generator-rectifier power supply at the WHMFC. The 100 MW/100 MJ pulsed generator is connected to the Rectifier Power Supply (RPS) through a 400 meter cable.  $L_1$  and  $R_1$  are the inductance and resistance of the cable. The RPS consists of two 67.5 MVA 12-pulse rectifiers which can operate independently as well as in parallel or in series [8]. The AC voltage of the pulsed generator is converted to DC voltage through the RPS to charge the magnet. By adjusting the firing angles of the RPS, a flat top current can be obtained in the magnet to achieve the desired flat top field.

2.2. Pulsed Generator

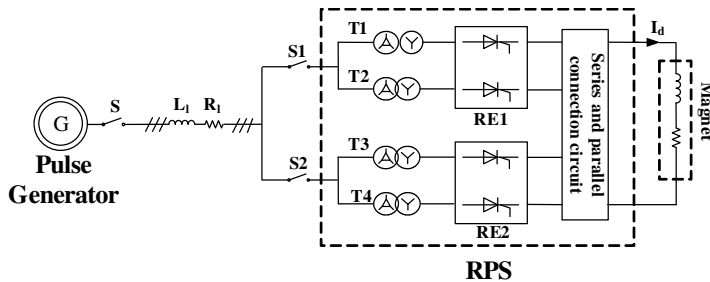
The parameters of the generator are shown in Table 1.

Table 1. Parameters of the pulsed generator.

Number of pole-pairs p	8	Saturated reactances at 66 Hz (PU)			
Peak power (pulse) at 0.8 PF	100 MVA	$X_d$	2.35	$X_q$	1.44
Frequency	94 to 66 Hz	$X'_d$	0.466	$X'_q$	1.44
Voltage	6900 V	$X''_d$	0.271	$X''_q$	0.333

The motor-generator, formerly operated in the USA, was dismantled and shipped to China in 2004. Because of the grid difference between China (50 Hz) and the USA (60 Hz), the maximum rotating speed of the flywheel is only 5/6 of the designed value. Therefore the maximum frequency of the generator terminal voltage is about 80 Hz at the WHMFC. However, with a forthcoming double-feed speed modification, the rotating speed and other parameters of the motor-generator will be increased up to the designed values.

According to [9], the motor-generator in Figure 1 can be replaced by an idealized equivalent three-phase voltage source  $V_N$  in series with an equivalent inductance  $L_{IN}$ , which is shown in Figure 2.  $L_{IN}$  is related to the direct-axis and quadrature-axis subtransient reactances  $X_d''$  and  $X_q''$  [9]. According to calculation and simulation results,  $L_{IN}$  is set to be 400  $\mu\text{H}$ .



**Figure 1.** Circuit diagram of the generator-rectifier power supply.

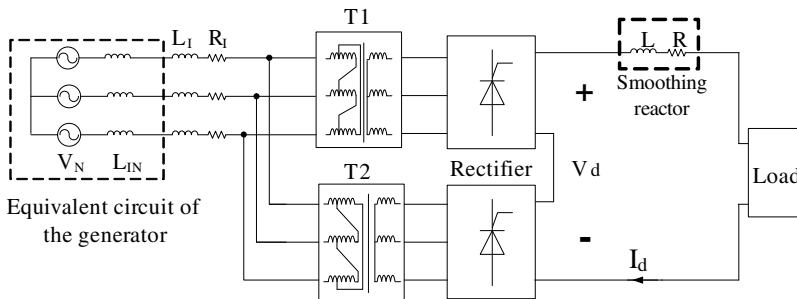


**Figure 2.** Equivalent circuit of the generator-rectifier power supply.

Equation (1) shows the relation between the available discharge energy  $E_{out}$  and the shaft speed  $\Omega_t$ .  $J$  is the inertia of the rotor and  $\Omega_N$  is the rotor speed before discharging. From (1) we can obtain  $\Omega_t$ . Once  $\Omega_t$  is obtained, the frequency  $f_G$  of the terminal voltage is

calculated by Equation (2).  $\Omega_t$  can be used to evaluate the amplitude of generator terminal voltage which is approximately proportional to  $f_G$ .

$$\frac{1}{2}J\Omega_N^2 - \frac{1}{2}J\Omega_t^2 = E_N - E_t = E_{out} \quad (1)$$

$$f_G = p\Omega_t = p\sqrt{(J\Omega_N^2 - 2E_{out})/J} \quad (2)$$

Figure 3 compares the simulated dc output currents of the detailed generator power supply of Figure 1 with the simplified equivalent power supply of Figure 2, with the other parameters of the two systems identical. We can see the relative error is less than 1% at the rated current of 25 kA.

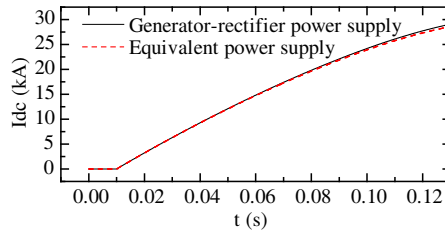


**Figure 3.** Output currents of the generator-rectifier power supply and the equivalent power supply.

### 2.3. Modeling of the 12-pulse Rectifier

An important characteristic of the 12-pulse rectifier power supply (RPS) is the Voltage Regulation Characteristic (VRC) that represents the link between the average dc output voltage  $V_d$  and the average dc output current  $I_d$  of the rectifiers. In general, the VRC of the 12-pulse RPS is related to the inductance  $L_t$  on the ac side of the RPS, the frequency and amplitude of the input voltage and the firing angle  $\alpha$  of the RPS.

To ensure the safe operation of the 12-pulse RPS, the minimum value of the firing angle  $\alpha$  is set to  $15^\circ$ . Due to the reactance  $X_t$  in the ac side of the RPS, it needs a certain time for the current in a conducting thyristor to be commutated to another thyristor which can affect the VRC of the RPS. The total reactance  $X_t$  consists of  $X_{IN}$ ,  $X_{Line}$  and the reactance  $X_r$  of the transformer which are shown in Figure 2.  $X_{IN}$  and  $X_{line}$  constitute the common commutation reactance  $X_c$  of the two 6-pulse rectifiers. Therefor  $X_c$  leads to a mutual interference between the two 6-pulse rectifiers. Then the VRC is closely related to  $X_t$  as well as the ration  $X_c$  to  $X_t$ . Parameters of

**Table 2.** Parameters of the transformers.

$S_N$ (MVA)	$f_N$ (Hz)	$V_{1N}$	$V_{2N}$	Short-Circuit Impedance $X_{short}$
10	80	6.9 kV	1.0 kV	3.8%

the transformers are listed in Table 2.  $L_{Line}$  is  $37.5 \mu\text{H}$ . Viewed from the secondary side of the transformer,  $X_c$  and  $X_t$  are calculated by Equation (3) at the normal frequency of 80 Hz.

$$\begin{aligned}
 X_c &= (X_{IN} + X_{Line}) \cdot (1/6.9)^2 \\
 &= (2\pi f_N L_{IN} + 2\pi f_N L_{Line}) \cdot (1/6.9)^2 = 4.6 \text{ m}\Omega \\
 X_r &= V_{1N}^2 / S_N \cdot X_{short} \cdot (1/6.9)^2 = 3.8 \text{ m}\Omega \\
 X_t &= X_c + X_r = 8.4 \text{ m}\Omega
 \end{aligned} \tag{3}$$

The ratio of  $X_c$  to  $X_t$  is:

$$A = X_c / (X_c + X_t) = 4.6 / (4.6 + 3.8) = 0.5476 \tag{4}$$

During the commutation intervals, there are generally three thyristors in contemporary conduction and the output dc voltage  $V_d$  descends linearity with the output dc current  $I_d$  due to the inductive voltage drop on  $X_c$  and  $X_r$ . The commutating time (the time required for commutating off full load current from a conducting thyristor) is proportional to the output dc current  $I_d$ . When  $I_d$  increases to a certain extent, the number of the thyristors conducting contemporarily can increase to 4, 5 or 6 and the operating mode of the 12-pulse power supply changes. Thus the VRC can be divided into several ranges according the different operating modes of the 12-pulse RPS. Equation (5) shows the expressions for the different ranges when the rectifiers are fired at the minimum allowable firing angle of  $15^\circ$ .

$$\left\{ \begin{array}{ll} V_d^* = 2 (\cos \alpha_{\min} - I_d^* / \sqrt{3}); & 0 \leq I_d^* \leq 0.223 \\ \frac{V_d^{*2}}{4 \cos^2 15^\circ} + \frac{I_d^{*2}}{3 \sin^2 15^\circ} = 1; & 0.223 \leq I_d^* \leq 0.2697 \\ V_d^* = 2.418 - 3.245 I_d^*; & 0.2697 \leq I_d^* \leq 0.463 \\ (0.5478 \cdot V_d^*)^2 + (2.0457 I_d^*)^2 = 1; & 0.463 \leq I_d^* \leq 0.5499 \end{array} \right. \tag{5}$$

$V_d^*$  and  $I_d^*$  are the normalized values of  $V_d$  and  $I_d$ . Equation (6) shows the base voltage and base current, where  $E$  is the amplitude of the no-load phase voltage at the secondary side of the transformer. With the harmonics omitted, the active power  $P$  of the 12-pulse RPS is equal to the active power consumed by the DC load, which is calculated by Equation (7). The approximate power factor of the 12-pulse RPS is calculated by Equation (8).

$$V_{base} = 3\sqrt{3}E/\pi, \quad I_{base} = E/X_t \quad (6)$$

$$P = V_d I_d \quad (7)$$

$$\cos \phi \approx \cos(\alpha + \mu_1/2) \quad (8)$$

The commutation angle  $\mu_1$  and firing angle  $\alpha$  in Equation (8) are related to the output dc current  $I_d$ . According to Equations (7) and (8), the apparent power is:

$$S = P / \cos \phi \quad (9)$$

#### 2.4. Constraints of the Power Supply

According to the descriptions above, there are mainly two constraints of the power supply. The dc load voltage should be less than the maximum output dc voltage of the 12-pulse RPS and the apparent power should be below the maximum power available. Both constraints are related to the frequency  $f_G$  which is calculated in Equation (2).

According to Equation (5), the maximum  $V_d$ - $I_d$  curve is presented in Figure 4. The green and black curves are the VRC of the power supply at 72 Hz and 80 Hz respectively. According to Equations (5)–(9), the maximum power-current curve is shown in Figure 5. The shaded areas in Figure 4 and Figure 5 are the feasible design regions of the 12-pulse RPS. When the frequency  $f_G$  of the generator terminal voltage is decreased the feasible design region shrinks. The green shading in Figure 4 and Figure 5 show the feasible design regions when  $f_G$  is decreased to 72 Hz.

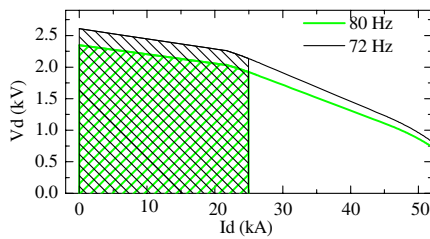


**Figure 4.**  $V_d$ - $I_d$  curves and feasible design regions at different power frequencies.

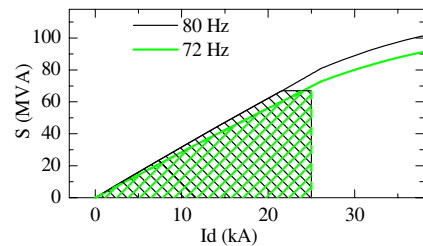


**Figure 5.** Power-current curves and feasible design regions at different power frequencies.

### 3. MATHEMATICAL MODEL OF THE MAGNET

#### 3.1. Introduction of the Quasi-continuous Magnet

Figure 6 shows a typical cross-section of a QCHMF magnet.  $H$ ,  $D_{out}$  and  $D_{in}$  are the height, outer diameter and inner diameter respectively. The magnet consists of several layers of conductor and reinforcing material. When the conductor is energized by the current from the power supply, a magnetic field proportional to the current is generated in the magnet.

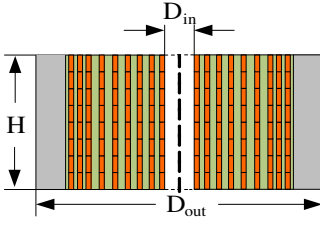


**Figure 6.** Cross-section of a quasi-continuous magnet.

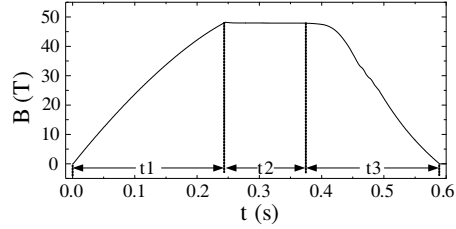


**Figure 7.** A typical quasi-continuous magnetic field curve.

Figure 7 shows a typical QCHMF curve. Due to the long pulse time and high magnetic field, the ohmic heating and magnetic force in the magnet are both very large. In addition, the current, voltage and power of the magnet should be within the normal operating regions of the power supply. Thus the magnet design needs to be optimized to satisfy all the constraints.

The magnetic field  $B$  in the center of a magnet shown in Figure 6 is determined by the volume of the conductors, the current density  $j$ , the inner diameter and the shape of the magnet. Magnet shapes varies with different values of  $D_{out}$  and  $H$ . With the same volume of conductors and current density  $j$ ,  $B$  has a maximum value of  $B_{max}$  when  $D_{out}$  is 1.675 times of  $H$ .  $B_{max}$  is calculated by Equation (10) [10].

$$B_{max} = \mu_0 \lambda j \left( 0.495 V^{1/3} - D_{in}/2 \right) \quad (10)$$

where  $V$  is the total volume of the uniformly wound magnet,  $\lambda$  the filling factor which represents the ration of the volume of the conductors to  $V$ , and  $\mu_0$  the air permeability.

The following analyses of the magnets are all based on the special shape mentioned above. The dimension of the magnet is determined by two parameters  $D_{in}$  and  $D_{out}$  (or  $H$ ). Together with the current density  $j$ ,  $\lambda$  and the cross sectional area  $S_0$  of the conductor, all the other parameters of the magnet can be determined.



### 3.2. Thermal Analysis

According to [10], the average temperature  $T$  of the magnet during the pulse is calculated by Equation (11)

$$T = F(x)$$

$$x = \int_0^{tend} j^2(t)dt + x_0 \quad (11)$$

where  $x_0$  is an initial value determined by the thermal properties and initial temperature of the magnet conductor.  $x$  is the time integral of the square of current density  $j^2(t)$ .  $F(x)$  is a complex expression that demonstrates the relation between the magnet temperature  $T$  and  $x$ . Most magnets are wound with copper, thus this paper mainly discusses the magnet wound with pure copper. To reduce the temperature rise in the magnet, liquid nitrogen is adopted to cool the magnet to 77 K before the pulse. Figure 8 shows the  $T$ - $x$  curve of pure copper with an initial temperature of 77 K.

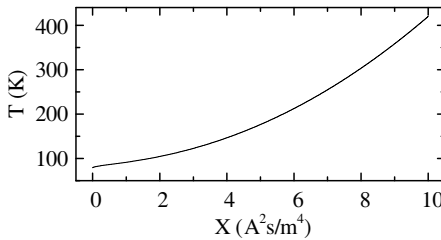


**Figure 8.**  $T$ - $x$  curve of copper with an initial temperature of 77 K.

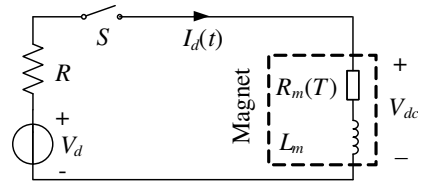


**Figure 9.** Equivalent circuit for the calculation of  $t_1$ .

The integral time  $tend$  in Equation (11) consists of the rise time  $t_1$ , flat top time  $t_2$  and fall time  $t_3$  which are shown in Figure 7. The flat top time  $t_2$  is determined by the experiment requirements and a flat top of 0.1 s is sufficient for most experiments. The rise time  $t_1$  is calculated based on the equivalent circuit shown in Figure 9.  $R$  is the resistance of the smoothing reactor. The value of  $V_d$  is related to the frequency  $f_G$  and the dc output current  $I_d(t)$  which is detailed in Section 2. The values of  $f_G$ ,  $I_d$  and  $R_m$  are all varying during the pulse. Analytical expression for  $t_1$  is difficult to obtain. Thus the rising process is divided into many small steps. In every step, equivalent average value of  $V_d$ ,  $f_G$ ,  $I_d$  and  $R_m$  are adopted to get the approximate rise time  $t_{1n}$  in the step. Summing up  $t_{1n}$  in each step, an approximate value of  $t_1$  is obtained, which is almost identical to the exact value of  $t_1$  if the

step is small enough. The fall time  $t_3$  can be obtained in the similar way. Once  $t_1$ ,  $t_2$  and  $t_3$  are obtained, the maximum temperature in the magnet can be derived from Equation (11).

Due to the magneto-resistance and skin effect, the maximum temperature in the magnet is higher than the average temperature derived from Equation (11). The accurate temperature distribution in the magnet can be calculated by finite element analysis.

### 3.3. Resistance and Inductance of Magnet

The resistance and inductance of the magnet are both closely related to the number of turns of the conductor in the magnet which is calculated by Equation (12).

$$N = H(D_{out} - D_{in})\lambda / (2S_0) \quad (12)$$

The resistance of the magnet is given by Equation (13).

$$R_m = \rho \frac{l}{s_0} = \frac{\pi N^2 (D_{out} + D_{in}) \rho}{H(D_{out} - D_{in}) \lambda} \quad (13)$$

The resistivity of the conductor  $\rho$  is related to temperature  $T$  of the magnet which is calculated by Equation (11). As for pure copper, the resistivity  $\rho$  is given by Equation (14).

$$\rho = -3.41e^{-9} + 7.2e^{-11} \cdot T \quad (14)$$

$R_m$  in Equation (13) is the average resistance of the magnet. When considering the magneto-resistance and the uneven temperature distribution in the magnet. The resistance should be corrected by a correction coefficient  $\rho_{correction}$ . An empirical value of  $\rho_{correction}$  for copper is 1.25.

The inductance is given by Equation (15).

$$L = 0.1447\mu_0 N^2 (D_{in} + D_{out}) \quad (15)$$

Equation (15) is correct when the conductor layers are uniformly distributed in the magnet. However, the thickness of the reinforcing layers has to be adjusted to achieve an optimized stress distribution throughout the coil. Then the distribution of conductor layers is not even. Thus  $L$  should be corrected by a correction factor  $K_{correct}$ . When the magnet is wound with copper and glass fiber,  $K_{correct}$  is set as 1.06 and the more precise value of  $L$  is calculated by Equation (16).

$$L = 0.1447\mu_0 N^2 (D_{in} + D_{out}) \cdot K_{correct} \quad (16)$$

### 3.4. Power and Energy

The maximum power consumed by the magnet is given by Equation (17).

$$P_m = V_m I_m = I_m^2 R_{mend} = (js_0)^2 R_{mend} \quad (17)$$

$R_{mend}$  is the resistance of the magnet at the end of the flat top. The energy in the magnet comprises the ohmic heat  $E_{heat}$  and the magnetic energy  $E_{mag}$ .  $E_{mag}$  and  $E_{heat}$  are given by Equations (18) and (19). The function  $f_{ET}$  (T) in Equation (19) describes the energy consumed by per kilogram of conductor when the temperature increases from a certain initial temperature to  $T$ , which is very complex. For pure copper with a 77 K initial temperature, the curve of the function  $f_{ET}$  (T) is shown by Figure 10.

$$E_{mag} = \frac{1}{2} L I_m^2 = \frac{1}{2} L (js_0)^2 \quad (18)$$

$$E_{heat} = M \cdot f_{ET}(T) \quad (19)$$

$$E_m = E_{heat} + E_{mag} \quad (20)$$

where  $M$  is the mass of the conductor in the magnet and  $E_m$  the total energy in the magnet which is equal to  $E_{out}$  in Equation (1) when ignoring the energy loss in other equipment of the power supply.

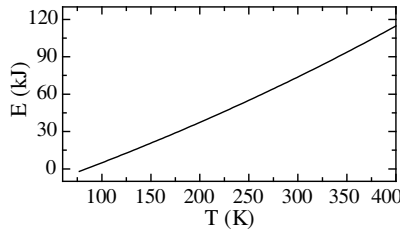


**Figure 10.** The curve of  $f_{ET}$  (T) for copper at a 77 K initial temperature.

### 3.5. Stress Constraints

Stress analysis is the most important and complex issue in the design and development of high field magnets. The optimization technology for internal reinforcement invented at the K. U. Leuven was proved to be an effective method and is used at almost all pulsed field laboratories worldwide [11]. However, the high strength reinforcing fiber composites reduce both the filling factor  $\lambda$  and thermal conduction of the coil. Thus the thickness of the reinforcing layers should be optimized

to balance the mechanical performance and filling factor  $\lambda$  of the magnet. Generally, the optimized filling factor  $\lambda$  of a certain magnet is determined by the mechanical properties of both the conductor and the reinforcing material. In addition, the radial dimension, or the width  $W$ , of the rectangular cross section of the conductor can also affect  $\lambda$ . Without loss of generality, an empirical value of 4 mm is assigned to the width  $W$  in this paper to simplify the optimization. Then the filling factor  $\lambda$  is empirically related to the maximum field  $B$  in the quasi-continuous magnet. When the magnet is wound with pure copper and glass fiber composites, the empirical  $\lambda$ - $B$  curve is shown in Figure 11. The  $\lambda$ - $B$  curve is verified by FEA shown by red squares in Figure 11. In the finite element verification, the elastic-plastic behavior of the copper and the anisotropic properties of the reinforcing fibers are taken into consideration. The peak von Mises stress in the copper and reinforcing fibers are both less than the maximum allowable values. The curve in Figure 11 forges an approximate mathematical link between the stress constraints and the maximum field  $B$  through the filling factor  $\lambda$ , which is adopted in the optimization process.

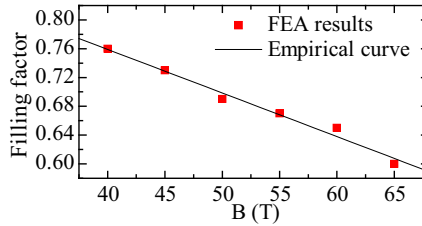


**Figure 11.**  $\lambda$ - $B$  curve of quasi-continuous magnet wound with copper and glass fiber.

## 4. OPTIMIZATION PROCESS AND SIMULATION VERIFICATION

### 4.1. Optimization Process

Optimization of QCHMF systems is a complicated non-linear process. Many parameters of the system are mutual dependent. To simplify the optimization, the magnet bore size  $D_{in}$  and the flat top time  $t_2$  are set as 22 mm and 0.1 s according to most experiment requirements. Then the independent variables of the optimization problem are the outer radius of the magnet  $a_2$  (or the outer diameter  $D_{out}$ ), the peak field  $B$  and the cross sectional area  $S_0$ . The three design variables constitute a 3-dimensional design space.

The magnet and the power supply both have to meet some design constraints such as the temperature rise, the magnetic force, the level of processing and the capacity of the power supply. Also the optimization objective can be various such as the highest field, the lowest power, the lowest temperature rise and the lowest cost. Thus, obtaining suitable designs of QCHMF system is a multi-objective problem. This means it is necessary to look for a solution in the design space that balances several objectives in the performance space. Generally, these objectives are conflicting, that is, there is no simultaneous optimal solution for all of them. The solution is not unique; instead there is a set of possible solutions where none is best for all objectives. This set of optimal solutions in the design space is called the Pareto set. The region defined by the performances (the value of all objectives) for all Pareto set points is called the Pareto front. Many algorithms can be utilized to produce the Pareto front [12–15]. Because our optimization problem has only three design variables whose variation ranges are relatively small, the Pareto front is produced through a simple traversal algorithm in this paper. Most efforts were put into choosing the most-preferred solution in the Pareto front.

To evaluate the points of the Pareto front, every objective is normalized by Equation (21). Then the constraints of the magnet and the power supply are translated to the objectives shown in Equation (22).

$$\begin{aligned} V_{norm} &= V_m/V_d; \quad I_{norm} = I_m/I_{max}; \quad S_{norm} = S/S_{max}; \\ B_{norm} &= \frac{B_{max}-B_{min}+0.5}{B-B_{min}+0.5} - 1; \quad T_{norm} = \frac{(T_{end}-77)}{(T_{end\ max}-77)}; \end{aligned} \quad (21)$$

$$V_{norm} < 1, \quad T_{norm} < 1, \quad I_{norm} < 1, \quad S_{norm} < 1 \quad (22)$$

$$Norm = V_{norm} + I_{norm} + S_{norm} + B_{norm} + T_{norm} \quad (23)$$

A normalized objective calculated by Equation (23) is used to evaluate the Pareto points. Every objective and design variable have its own graphical representation. The visual representation of the Pareto front is shown in Figure 12. The vertical axis of all graphs corresponds to the norm obtained in Equation (23).

Among these points, a good choice is the point associated with the lowest norm which is shown by the pink pentagram.

Table 3 shows the values of the normalized objectives and design

**Table 3.** Values of objectives and variables of the point with the lowest norm.

$S_{norm}$	$B_{norm}$	$T_{norm}$	$I_{norm}$	$V_{norm}$	$B$ (T)	$a_2$ (cm)	$s_0$ (mm <sup>2</sup> )
0.768	0.406	0.711	0.97	0.992	50.7	18.06	50.9

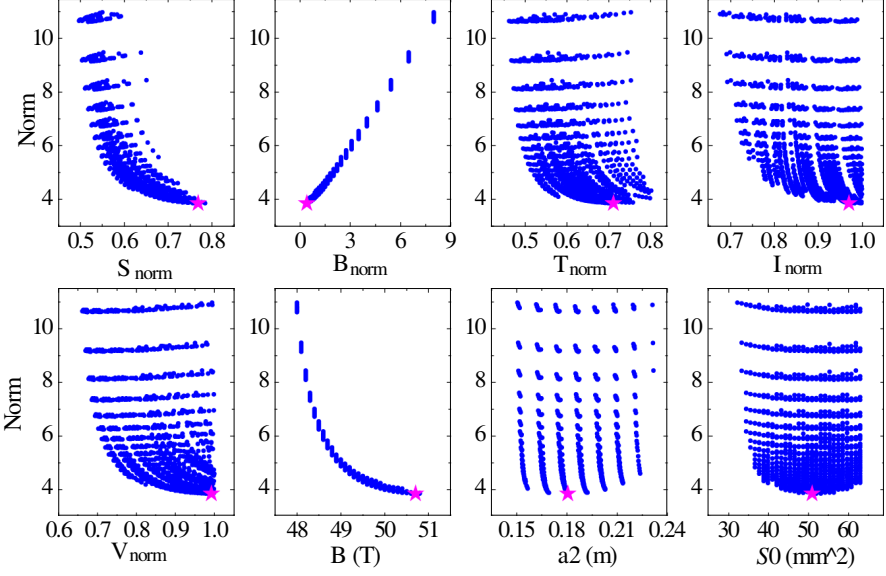


**Figure 12.** Visual representation of the Pareto front.

variables of the chosen point with the lowest norm. The chosen point has enough margins in the power and the temperature to achieve a 50.7 T/0.1 s T QCHMF. However, the current and voltage of the chosen point are too close to the maximum allowable values of the power supply, which gives little flexibility and reliability to the design. Thus the point with the lowest norm may not be the preferred solution. To obtain a more preferred one, the graphical representation, combined with a coloring methodology of the points based on preferences of the designer, is adopted [16].

The Pareto points have different values for each objective that can be divided into several ranges according to the classification in Table 4. In Table 4, six regions are defined for each objective that delineates degrees of desirability: Highly Desirable (*HD*), Desirable (*D*), Tolerable (*T*), Undesirable (*U*), Highly Undesirable (*HU*) and Unacceptable (*UNA*). According to the classification, a scoring system shown in Table 5 is established. The proposed system follows the ‘ones vs others’ criteria established by Messac [17].

The coefficient  $k_1$ ,  $k_2$ ,  $k_3$  and  $k_4$  are calculated in Equation (24).

$$k_i = \frac{J_n - J_n(i)_{\min}}{J_n(i)_{\max} - J_n(i)_{\min}}, \quad i = 1, 2, 3, 4, 5, 6 \quad (24)$$

where  $J_n$  denotes the objectives such as  $S$ ,  $B$ ,  $T_{end}$ ,  $I_m$  and  $V_{norm}$ .

**Table 4.** Classification of the objectives.

	$S$ (MVA)	$B$ (T)	$T_{end}$ (K)	$I_m$ (kA)	$V_{norm}$
$HD$	(0, 33.75)	(52, $+\infty$ )	(77, 200)	(0, 12)	(0, 0.5)
$D$	(33.75, 47.25)	(50, 52)	(200, 250)	(12, 17)	(0.5, 0.7)
$T$	(47.25, 57.38)	(48, 50)	(250, 280)	(17, 23)	(0.7, 0.9)
$U$	(57.38, 64.13)	(46, 48)	(280, 300)	(23, 24.5)	(0.9, 0.95)
$HU$	(64.13, 67.5)	(45, 46)	(300, 350)	(24.5, 25)	(0.95, 1)
$UNA$	(67.5, $+\infty$ )	(0, 45)	(350, $+\infty$ )	(25, $+\infty$ )	(1, $+\infty$ )

**Table 5.** Scoring system for the Pareto points.

class	$HD$	$D$	$T$	$U$	$HU$	$UNA$
score	0	$1 + 1 * k_1$	$11 + 10 * k_2$	$106 + 50 * k_3$	$781 + 100 * k_4$	4406

$J_n(i)_{\max}$  and  $J_n(i)_{\min}$  are the boundaries of the  $i$ -th class of a certain objective  $J_n$ .

According to the scoring system, every objective of a certain Pareto point has a score. Summing all the scores of the objectives, a total score is obtained for each Pareto point. For example, a point  $P$  with the objective values of (40 MVA, 50.8 T, 230 K, 23.5 kA, 0.85) has a vector of score of (1.46, 1.6, 1.6, 122.67, 18.5) and a total score of 145.83.

Once the total scores of all the Pareto points are obtained with the scoring system, the color is then assigned according to the score of each point. The resulting colored Pareto points are shown in Figure 13. Actually, Figure 13 only shows the points that can achieve field over 50 T, which is very preferred. A redder color means a lower score and so a better point. The designer can choose one of the redder points, for instance, the point with the lowest score (the black pentagram in Figure 13). Table 6 shows the values of the normalized objectives and the key parameters of the chosen point.

**Table 6.** Values of objectives and parameters of the Pareto point with the lowest score.

$S_{norm}$	$B_{norm}$	$T_{norm}$	$I_{norm}$	$V_{norm}$	$B$ (T)	$a_2$ (cm)	$s_0$ (mm <sup>2</sup> )
0.69	0.8	0.65	0.95	0.898	50	17.92	50.9

It can be concluded that the point with the lowest score in Table 6 can achieve a field almost as high as the point with the lowest norm in Table 5 with all the objectives having sufficient margins.





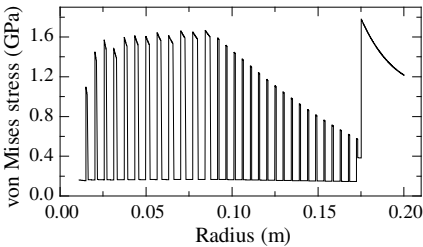


**Figure 14.** Von Mises stress at the mid-plane of the magnet at the peak field.

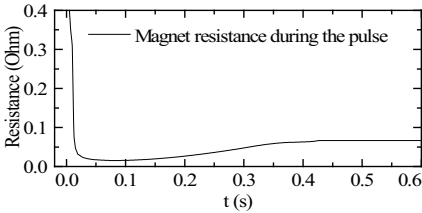


**Figure 15.** Resistance curve during the pulse.

stress in the middle-plane of the magnet is shown in Figure 14. The maximum von Mises stress is below 165 MPa in the copper wire and less than 1.7 GPa in the glass fiber composite, which are below the UTS of the copper (300 MPa) and the glass fiber/epoxy composite (2.6 GPa) respectively.

**Table 7.** Parameters of the optimized magnet.

Resistance (77 K)	Inductance	Height	Mass of copper	Peak current
12.4 mΩ	16.1 mH	20.57 cm	130.4 kg	23.85 kA

The specific internal structure of the magnet is derived according to the optimized thickness of the reinforcing layers. Then the exact resistance  $R_{FEA}$  (77 K) and inductance  $L_{FEA}$  derived from the FEA of the magnet are shown in Equation (25) which are very close to the values list in Table 7.

$$R_{FEA} = 12.4\text{ m}\Omega, \quad L_{FEA} = 16.1\text{ mH}$$

(25)

A simulation model of the power supply system was built with Matlab/Simulink. The model is based on the circuit diagram in Figure 1. To model the generator, the Synchronous Machine pu Standard block is adopted. All the parameters of the block are specified according to the values in Table 1. Other elements such as the connecting cables, transformers and rectifiers are all based on the parameters in the article. Since the resistance of the magnet is varying due to joule heat, the magneto resistance and the skin effect during the pulse, which is hard to be considered in Matlab. An electro-thermal finite element analysis is performed to get the varying resistance of the magnet in COMSOL. The magnet model in COMSOL is energized by the flat top pulse current with the rise time  $t_1$  and fall time  $t_3$  derived from Section 3.2. Figure 15 shows the curve of the obtained

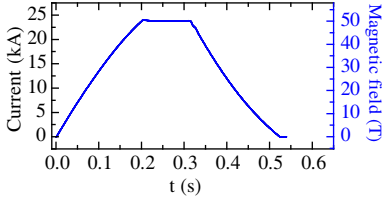


**Figure 16.** Current (magnetic field) curve of the optimized QCHMF.

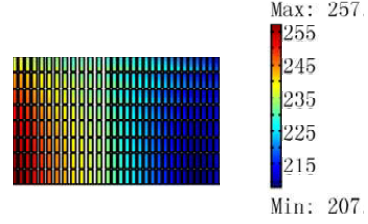


**Figure 17.** Temperature distribution in a quarter cross-section of the magnet after the pulse.

varying resistance  $R_{m\_vary}$  of the magnet. During the pulse, the magnet inductance remains constant at  $L_{FEA}$ . Once  $R_{m\_vary}$  and  $L_{FEA}$  are obtained, the exact flat top current curve through the magnet can be easily derived. To maintain the flat-top current of the magnet coil a constant value for 100 ms, a current feedback loop with a PI-controller is integrated in the power supply control system, where the firing angles of the rectifiers are adjusted according to the error between the measured coil current and the reference value. Figure 16 shows the obtained flat top current curve of the magnet, which can be used to calculate the temperature rise of the magnet in COMSOL. Figure 17 shows that the highest temperature in the magnet after the pulse is 257 K, which is safe for the reinforcing and insulating materials in the magnet. According to the simulation results of Matlab/Simulink, the maximum output power is about 45 MVA that is much less than 67.5 MVA. Therefore, both the magnet and the power supply of the optimized QCHMF system have enough margins to achieve the designed 50 T/100 ms QCHMF.

## 5. CONCLUSIONS

A generic coupling model of the QCHMF system considering the constraints of the magnet and the power supply system is proposed. The design of QCHMF systems is formulated as a five-objective problem and a coloring methodology based on the preferences of the designer is adopted to get the graphical representation of the Pareto front of the optimization problem. According to the proposed model and optimization method, an optimized 50 T/100 ms QCHMF design is obtained. Simulations using Matlab and Comsol verified that the optimized system can achieve the designed QCHMF with all the constraints satisfied and can balance all the objectives. With different preferences incorporated in the optimization methodology, other different optimized designs can be obtained. Also, the proposed

coupling model of the QCHMF system and the optimization method can be easily adapted to other QCHMF systems with hybrid power supplies or multi-coil magnets to achieve higher QCHMF in the future.

## ACKNOWLEDGMENT

The authors would like to acknowledge the financial support from the National Natural Science Foundation of China (No. 51177062).

## REFERENCES

1. Jaime, M., R. Movshovich, G. R. Stewart, W. P. Beyermann, M. G. Berisso, M. F. Hundley, P. C. Canfield, and J. L. Sarrao, "Closing the spin gap in the Kondo insulator  $\text{Ce}_3\text{Bi}_4\text{Pt}_3$  at high magnetic fields," *Nature*, Vol. 405, 160–163, May 2000.
2. Sun, F. and S. He, "Create a uniform static magnetic field over 50 T in a large free space region," *Progress In Electromagnetics Research*, Vol. 137, 149–157, 2013.
3. Ravaut, R. and G. Lemarquand, "Magnetic field in MRI yokeless devices: Analytical approach," *Progress In Electromagnetics Research*, Vol. 94, 327–341, 2009.
4. Gersdorf, R., L. W. Roeland, and W. Mattens, "A magnet for semi-continuous fields up to 60 T," *IEEE Trans. Magn.*, Vol. 24, 1052–1054, 1988.
5. Sims, J. R., J. B. Schillig, G. S. Boebinger, H. Coe, A. W. Paris, M. J. Gordon, M. D. Pacheco, T. G. Abeln, R. G. Hoagland, M. C. Mataya, K. Han, and A. Ishmaku, "The U. S. NHMFL 60 T long pulse magnet failure," *IEEE Trans. Appl. Supercond.*, Vol. 12, 480–483, 2002.
6. Singleton, J., C. H. Mielke, A. Migliori, G. S. Boebinger, and A. H. Lacerda, "The national high magnetic field laboratory pulsed-field facility at Los Alamos National Laboratory," *Physica B*, Vol. 346, 614–617, 2004.
7. Groessinger, R., M. Schonhart, M. Kriegisch, M. Haas, and H. Sassik, "High field facilities at TU Vienna," *J. Low Temp. Phys.*, Vol. 159, 394–401, 2010.
8. Ding, H., J. Hu, W. Liu, Y. Xu, C. Jiang, T. Ding, L. Li, X. Duan, and Y. Pan, "Design of a 135 MW power supply for a 50 T pulsed magnet," *IEEE Trans. Appl. Supercond.*, Vol. 22, 5400504–5400504, 2012.
9. Weiming, M., H. An, L. Dezhi, and Z. Gaifan, "Stability of a synchronous generator with diode-bridge rectifier and back-EMF

- load,” *IEEE Trans. Energy Convers.*, Vol. 15, No. 4, 458–463, 2000.
10. Gersdorf, R., F. A. Muller, and L. W. Roeland, “Design of high field magnet coils for long pulses,” *Rev. Sci. Instrum.*, Vol. 36, 1100–1109, 1965.
  11. Herlach, F., K. Rosseel, and J. Vanacken, “Frontiers of pulsed magnet design,” *IEEE Trans. Appl. Supercond.*, Vol. 14, 1229–1232, 2004.
  12. Goudos, S. K., K. Siakavara, E. Vafiadis, and J. N. Sahalos, “Pareto optimal Yagi-Uda antenna design using multi-objective differential evolution,” *Progress In Electromagnetics Research*, Vol. 105, 231–251, 2010.
  13. Touati, S., R. Ibtouen, O. Touhami, and A. Djerdir, “Experimental investigation and optimization of permanent magnet motor based on coupling boundary element method with permeances network,” *Progress In Electromagnetics Research*, Vol. 111, 71–90, 2011.
  14. Zhang, Z. and Y. H. Lee, “A robust cad tool for integrated design of UWB antenna system,” *Progress In Electromagnetics Research*, Vol. 112, 441–457, 2011.
  15. Huang, M., S. Yang, J. Teng, Q. Zhu, and Z.-P. Nie, “Multiobjective optimization and design of a Luneberg lens antenna with multiband multi-polarized feed-system,” *Progress In Electromagnetics Research*, Vol. 129, 251–269, 2012.
  16. Blasco, X., J. M. Herrero, J. Sanchis, and M. Martínez, “A new graphical visualization of n-dimensional Pareto front for decision making in multiobjective optimization,” *Inform. Sciences*, Vol. 178, 3908–3924, 2008.
  17. Messac, A., “Physical programming: Effective optimization for computational design,” *AIAA Journal*, Vol. 34, 149–158, 1996.